Transmitter Adaptation and Wireless Power Control for Capsule Endoscopy

Heng Zhang, *Graduate Student Member, IEEE*, Zheng Li, *Senior Member, IEEE*, and Chi-Kwan Lee, *Senior Member, IEEE*

***Abstract*—Inductive coupling, a form of wireless power transfer (WPT) offers a promising solution for enabling wireless capsule endoscopes (WCEs) when direct wire connections are impractical. In this approach, a 1-D receiving coil is integrated into a WCE, which is positioned within the stomach. Simultaneously, a 3-D transmitting coil (3DTC) is constructed outside the human body to provide the necessary power for the operation of the WCE. The WPT system described in this article is the first complete prototype wherein the receiving coil is integrated within a fully functional WCE and capable of accommodating an adult human body with the 3DTC. Mathematical analysis and computer simulations have verified the magnetic field direction at the center of the 3DTC can be precisely controlled to any orientation by manipulating the 3DTC currents. The static measurements of the WCE-received power at various angles from 0° to 180° range between 1210 mW and 1822.5 mW, which are all above the power requirement of typical WCEs. In the subsequent adaptive test, the inertial measurement unit in the WCE collects the orientation information of the capsule and, then, wirelessly transmits it to the microcontroller unit of the 3DTC controlling the coils' excitation. It is confirmed that the proposed system is able to control the coil excitation following the capsule rotation as it would within the human stomach.**

***Index Terms*—3-D transmitting coil (3DTC), capsule endoscope, wireless power transfer (WPT).**

Acronyms and Abbreviations

WCE	Wireless capsule endoscope.
GI	Gastrointestinal.
WPT	Wireless power transfer.
PTE	Power transfer efficiency.
RPS	Received power stability.
MCU	Microcontroller unit.
RMS	Root mean square.
BLE	Bluetooth Low Energy.
ADC	Analog-to-Digital Converter.
PCB	Printed circuit board.
AV	Audio and Video.
IMU	Inertial measurement unit.
DRC	Dimensional receiving coil.
DTC	Dimensional transmitting coil.
SAR	Specific absorption rate.
EMF	Electromagnetic field.

Manuscript received 29 August 2023; revised 15 November 2023; accepted 15 December 2023. Date of publication 9 January 2024; date of current version 16 February 2024. This work was supported by the Hong Kong Research Grant Council under the General Research Fund Projects 17210420 and 17213423 and Theme-Based Research Scheme T23-701/20-R. Recommended for publication by Associate Editor A. Safaee. *(Corresponding author: Chi-Kwan Lee.)*

Heng Zhang and Chi-Kwan Lee are with the Department of Electrical and Electronic Engineering, The University of Hong Kong, Hong Kong (e-mail: zhhku@connect.hku.hk; cklee@eee.hku.hk).

Zheng Li is with the Department of Surgery, Chow Yuk Ho Technology Centre for Innovative Medicine, The Chinese University of Hong Kong, Hong Kong, also with the Li Ka Shing Institute of Health Science, The Chinese University of Hong Kong, Sha Tin, Hong Kong, and also with the Multi-scale Medical Robotics Centre, Ltd., The Chinese University of Hong Kong, Hong Kong (e-mail: lizheng@cuhk.edu.hk).

Color versions of one or more figures in this article are available at https://doi.org/10.1109/TPEL.2023.3345277.

Digital Object Identifier 10.1109/TPEL.2023.3345277

I. Introduction

STOMACH cancer is the primary health challenge with a high incidence and mortality, causing approximately 0.76 million deaths in 2020 all over the world [1]. WCE has become a preferred diagnostic device for diagnosing the diseases of GI tract since its invention due to its characteristics of noninvasive and painless [2], [3], [4]. Through swallowing a pill-sized capsule, gastric abnormalities such as polyps, ulcers, bleeding, and infections can be detected in patients and diagnosed by surgeons through wireless video transmission [5], [6], [7]. Such a procedure has become a favored clinical diagnosis for specific diseases, such as Crohn's disease [8], [9].

In order to improve the diagnostic quality, several key specifications of the WCE, such as image resolution, frame rate, and operating time, are required to be improved, which will consume more energy [10]. In the future, capsules will not only be limited to the detection of images but will also involve multiple tasks (e.g., biopsy, drug release, and self-dependent movement) [11]. All these functions will increase power consumption, which cannot be satisfied by conventional battery power. When WCEs are designed as active robots that can perform multiple tasks, their power requirements are at least 420 mW [12]. As a result, the energy supply for the WCE has been a challenging issue, as the capsule is too small to carry a large-capacity battery, and a power wire can cause uncomfortable for patients or cannot allow the capsule to move freely [13]. WPT based on inductive coupling is a promising solution for the energy issue of WCE.

In recent years, a number of researchers have investigated the WPT of capsules. Sun et al. [14] introduced a novel two-hop WPT system with an efficiency-enhanced power receiver for motion-free capsule endoscopy inspection. The power is transmitted from the floor via a strong coupling to the power relay in the patient jacket. In the next step, power is transmitted from

the power relay to the capsule via a loose coupling. This method not only makes the patient more comfortable but also eliminates the source of reliability problems caused by moving cables and connectors. Basar et al. [15] proposed a method to improve the power stability and PTE of WCEs by a hybrid resonant scheme to improve PTE and a novel power transmission coil capable of generating a uniform magnetic field to improve power stability through uniform magnetic fields while minimizing unwanted peak electromagnetic exposure.

Basar et al. [16] proposed an effective WPT system that significantly improves the PTE and enriches the RPS. An optimal triple coil inductive link is used to improve the PTE with compact wearable power transmitting coils, which have been tested in four types and a 2-D to 3-D power receiving coil. Gao et al. [13] introduced a new WPT system for the stable power supply of capsules, mainly consisting of a rotatable 2-D transmitting coil(2DTC), a 1-D receiving coil (DRC), and an attitude detection module. It greatly reduces the size of the receiver coil mounted on the capsule, freeing up space for the capsule to be fitted with other equipment.

The receiving coils of the 3DRC schemes are too large and require more volume of the capsule endoscope. The scheme of rotatable 2DTC and 1DRC requires rotational mechanics for the transmitting coils. Therefore, the challenging issue is that reducing the receiving coil to 1DRC while the magnetic field direction of the transmitting coil can quickly track the direction of the receiving coil due to the fast motion of the capsule in the stomach. At the same time, the working space should be sufficient to accommodate the human body, and no matter in which direction, the power can be transmitted to the capsule.

In our group's past studies [17], we have investigated the omnidirectional power transfer capability of a 3DTC. Based on the previous challenges and our past research, in this article, we propose a capsule endoscope tracking WPT system with a 3DRC and 1DRC, combined with an attitude sensor IMU, to achieve a closed-loop WPT function. The principal contributions of this research are summarized as follows.

1) This article bridges the gap between scientific research and practical applications of WPT for capsule endoscopy. A decent 3DTC transmitter and a miniature capsule endoscope are designed and manufactured. The 3DTC transmitter is comfortable for accommodating an adult human body, and the capsule endoscope provides all the features for the diagnosis of GI diseases.
2) The experimental results were conducted in both static and attitude changing of the capsule endoscope. It is confirmed that the proposed self-adaptive control method is able to regulate the power in the transmitter, without disrupting the operation of the capsule endoscope.
3) The health issue of human exposure to EMF is preliminarily evaluated by determining the field strength and SAR through COMSOL simulation. The effectiveness and safety of WPT for capsule endoscopy in diagnosing GI diseases have been confirmed, making it a promising technology.

The rest of this article is organized as follows. Section II introduces the design of the 3DTC, 1DRC, and WCE. The magnetic field distribution of 3DTC is calculated, simulated, and measured in Section III. Section IV presents the circuit design for the control of the magnetic field of 3DTC. In Section V, static and self-adaptive WPT experiments are performed to verify the feasibility of the designed WPT system for WCE. The discussion is given in Section VI. Finally, Section VII concludes this article.

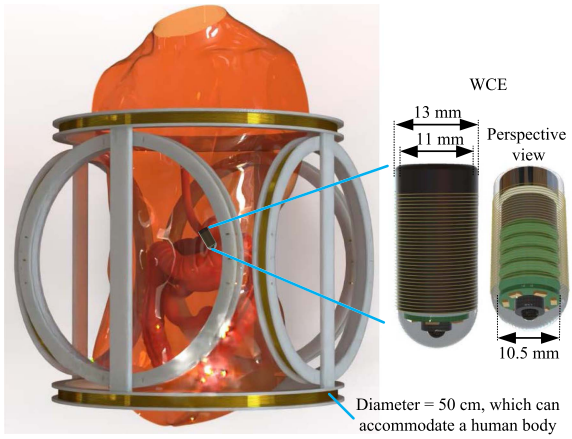

Fig. 1. System concept diagram for WPT of WCE.

II. System Design

This section briefly describes the design of the WPT system and the WCE. In order to achieve the function of a receiving coil wound around the capsule that can be charged at any angle, a structure of 3DTC suitable for the human body has been designed. As shown in Fig. 1, the 3DTC can generate a magnetic field in any direction in space, thus allowing the capsule to receive energy from the transmitting coil regardless of its attitude. The attitude of the capsule is measured by the IMU and sent to the master MCU via Bluetooth. The MCU controls the direction of the magnetic field in space by controlling the currents of the three sets of transmitting coils (or 3DTC).

The electronic architecture diagram of the WPT system is shown in Fig. 2. The MCU used is the STM32F103C8T6, which is responsible for generating PWMs to control the full-bridge circuit to change the current of each transmitting coil set and for obtaining the data of current sensors and the attitude of IMU. The current sensor converts the measured RMS value of the transmitting coil set current into a voltage value and connects it to the analog acquisition pin of the ADS1256, which is a 24-b high-precision ADC chip. The MCU obtains the current value of each transmitting coil by communicating with the ADS1256 to achieve closed-loop control of the current. In addition, the BLE slave obtains the IMU data to get the attitude data and transmits it to the MCU via the BLE master. Then, the MCU calculates the current value required for each transmitting coil set based on the attitude data to achieve the closed-loop control of the WPT.

A. Design of WPT Transmitting Coils

The configuration of the transmitting coils is illustrated in Fig. 3, wherein coils C_{X1} and C_{X2} are employed to generate a

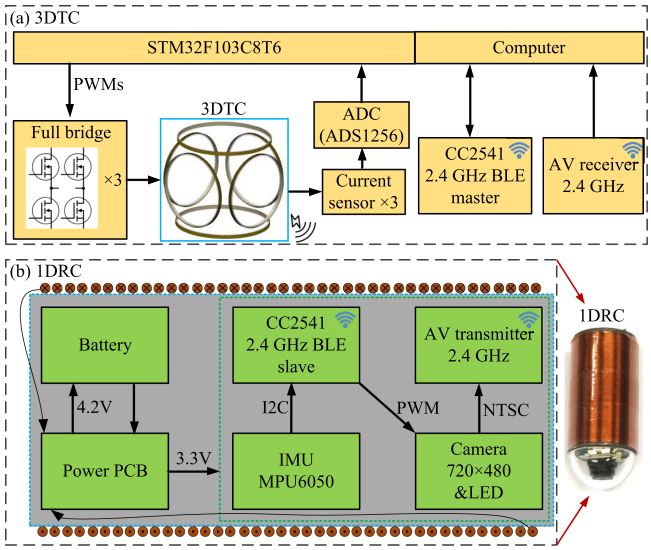

Fig. 2. Electronic architecture diagram of the WPT system. (a) 3DTC and the control part. (b) 1DRC in WCE.

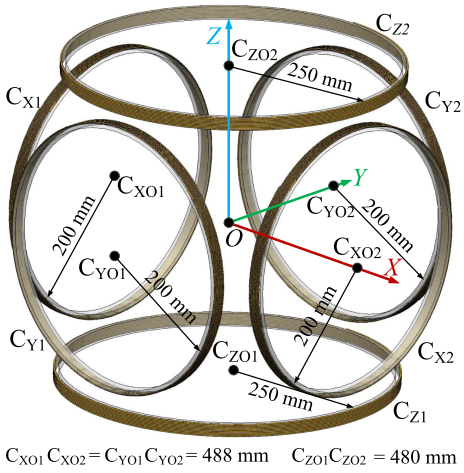

Fig. 3. Structure and dimensions of the 3DTC.

magnetic field along the x-axis, coils C_{Y1} and C_{Y2} are utilized for the y-axis, and coils C_{Z1} and C_{Z2} are applied for the z-axis. C_{XO1}, C_{XO2}, C_{YO1}, C_{YO2}, C_{ZO1}, and C_{ZO2} represent the centers of coils C_{X1}, C_{X2}, C_{Y1}, C_{Y2}, C_{Z1}, and C_{Z2}, respectively. The distances between C_{XO1} and C_{XO2}, C_{YO1} and C_{YO2}, and C_{ZO1} and C_{ZO2} are 488 mm, 488 mm, and 480 mm, respectively. The available space exceeds the width of the Boeing seat, which typically ranges from 17 to 18 in (431.8–457.2 mm) [18]. Based on this size, we designed the diameter of the transmitting coil in the z-axis direction and the transmitting coils in x and y axes to cover the human body as much as possible to achieve a more uniform magnetic field in the GI position. In order to make the magnetic field generated by the coils on the same axis at the point of coordinate O equal in magnitude and direction, the coils on the same axis have the same number of turns and are connected in series to ensure that the currents are equal. The parameters of transmitting coils are shown in Table I. The winding wire is

TABLE I
PARAMETERS OF THE TRANSMITTING COILS

Parameter	C_{X1}, C_{X2}, C_{Y1}, and C_{Y2}	C_{Z1} and C_{Z2}
Radius (cm)	20	25
Number of turns	28 (3 layers)	25 (3 layers)
Widths of sub-coils (cm)	2	2
Equivalent series inductance @218 kHz (μH)	900	1224

TABLE II
PARAMETERS OF THE TRANSMITTING COILS OF EACH AXIS WHEN CONNECTED IN SERIES

Parameter	C_{XX} or C_{YY}	C_{ZZ}
Equivalent series inductance @218 kHz (μH)	2152	2646
Equivalent series resistance @218 kHz (Ω)	23.34	44.98
Quality factor @218 kHz	126	81
Maximum Mutual inductance with WCE at O @218 kHz (μH)	18	25

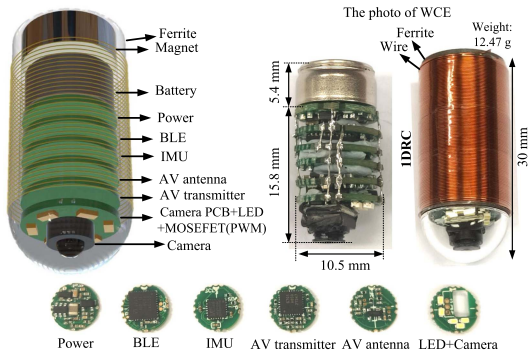

Fig. 4. Design and components of the WCE.

a Litz wire, with a diameter of 1.91 mm, constructed with 200 strands of AWG38 enameled copper wire.

The parameters of the coils in series for each axis are shown in Table II. C_{XX} refers to the combined coils of C_{X1} and C_{X2} in series, C_{YY} refers to C_{Y1} and C_{Y2} in series, and C_{ZZ} refers to C_{Z1} and C_{Z2} in series. Due to the mutual inductance, the inductance of the coils in series is greater than twice the inductance of the individual coils.

B. Design of WPT Receiving Coil

With reference to the capsule dimensions ϕ13 mm × 27.9 mm [19], we designed a custom-made PC40 ferrite ring ϕ13 mm × 24 mm. The ferrite ring has an 11-mm inner diameter to allow for the placement of circuit boards, a camera, a battery, a permanent magnet, and LEDs inside. The ferrite core can concentrate the magnetic flux and enhance the coupling [20]. The wire of the receiving coil is tightly wound on the surface of the ferrite ring, which in combination with the attitude data provided by the integrated IMU completes the tracking transmission of electrical energy. The receiving coil (1DRC) can be

TABLE III
PARAMETERS OF THE RECEIVING COIL

Parameter	Receiving coil
Winding enameled copper wire (mm)	0.19
Coil diameter (mm)	13.4
Number of turns	200 turns (2 layers)
Ferrite magnetic ring	PC40 (11-13)×24 mm
Equivalent series inductance @218 kHz (μH)	2160
Equivalent series resistance @218 kHz (Ω)	97.67
Quality factor @218 kHz	30

seen in Fig. 4. The parameters of the receiving coil are shown in Table III.

C. Design of WCE

The WCE is designed to screen stomach abnormalities under magnetic actuation, as shown in Fig. 4. The capsule primarily comprises six PCBs, a glass cover, a permanent magnet, a battery (LIR1054), and an annular ferrite. Specifically, these PCBs consist of a power converter, BLE, IMU, AV antenna, AV transmitter, and an LED-camera PCB. Among them, the power converter PCB can output a stable 3.3 V voltage from the battery by the chip of XC6206P332 to power other PCBs and a stable 4.2 V from WPT by a dc–dc converter (TPS54202) for charging the battery LIR1054. The core chip of the BLE PCB is the CC2541, which can be programmed in the C language to enable remote communication, data collection from the IMU, and control of LED brightness by PWM. For the IMU PCB, the MPU6050 chip, equipped with a three-axis accelerometer and a three-axis gyroscope, is selected to acquire the orientation angle of the capsule. The transmission of camera video is accomplished through the collaboration of two PCBs, an AV antenna, and an AV transmitter.

III. ANALYSIS OF MAGNETIC FIELD DISTRIBUTION

A. Principle of the 3DTC

The magnetic field generated by the 3DTC is excited by the drive current of the individual coil set along each axis. The driving currents in the x, y, and z axes are I_{x}, I_{y}, and I_{z}, respectively

$$\begin{aligned} I_{\mathrm{x}} &= |I_{\mathrm{x}}|\cos(\omega t+\varphi_{\mathrm{x}}) \\ I_{\mathrm{y}} &= |I_{\mathrm{y}}|\cos(\omega t+\varphi_{\mathrm{y}}) \\ I_{\mathrm{z}} &= |I_{\mathrm{z}}|\cos(\omega t+\varphi_{\mathrm{z}}) \end{aligned} \tag{1}$$

where ω is $2\pi \times 218$ kHz; φ_{x}, φ_{y}, and φ_{z} are the phase angles of I_{x}, I_{y}, and I_{z}, respectively. The phase angles controlled in this article are either 0° or 180°. The magnetic field excited at position $P(X,Y,Z)$, driven by I_{x}, I_{y}, and I_{z}, is $\boldsymbol{B}_{\mathrm{P}}(X,Y,Z)$. Its components in each axis are B_{x}, B_{y}, and B_{z} which can be expressed approximately in the central area of the 3DTC

$$\begin{aligned} B_{\mathrm{x}} &\approx \mu_0 N_{\mathrm{x}} I_{\mathrm{x}} \left(\int_0^{2\pi} \frac{{R_{\mathrm{x}}}^2 - R_{\mathrm{x}} Y\cos\theta_{\mathrm{x1}} - R_{\mathrm{x}} Z\sin\theta_{\mathrm{x1}}}{|\boldsymbol{v}_{\mathrm{x1p}}|^3} d\theta_{\mathrm{x1}} \right. \\ &\quad \left. + \int_0^{2\pi} \frac{{R_{\mathrm{x}}}^2 - R_{\mathrm{x}} Y\cos\theta_{\mathrm{x2}} - R_{\mathrm{x}} Z\sin\theta_{\mathrm{x2}}}{|\boldsymbol{v}_{\mathrm{x2p}}|^3} d\theta_{\mathrm{x2}} \right) \\ B_{\mathrm{y}} &\approx \mu_0 N_{\mathrm{y}} I_{\mathrm{y}} \left(\int_0^{2\pi} \frac{{R_{\mathrm{y}}}^2 - R_{\mathrm{y}} Z\cos\theta_{\mathrm{y1}} - R_{\mathrm{y}} X\sin\theta_{\mathrm{y1}}}{|\boldsymbol{v}_{\mathrm{y1p}}|^3} d\theta_{\mathrm{y1}} \right. \\ &\quad \left. + \int_0^{2\pi} \frac{{R_{\mathrm{y}}}^2 - R_{\mathrm{y}} Z\cos\theta_{\mathrm{y2}} - R_{\mathrm{y}} X\sin\theta_{\mathrm{y2}}}{|\boldsymbol{v}_{\mathrm{y2p}}|^3} d\theta_{\mathrm{y2}} \right) \\ B_{\mathrm{z}} &\approx \mu_0 N_{\mathrm{z}} I_{\mathrm{z}} \left(\int_0^{2\pi} \frac{{R_{\mathrm{z}}}^2 - R_{\mathrm{z}} X\cos\theta_{\mathrm{z1}} - R_{\mathrm{z}} Y\sin\theta_{\mathrm{z1}}}{|\boldsymbol{v}_{\mathrm{z1p}}|^3} d\theta_{\mathrm{z1}} \right. \\ &\quad \left. + \int_0^{2\pi} \frac{{R_{\mathrm{z}}}^2 - R_{\mathrm{z}} X\cos\theta_{\mathrm{z2}} - R_{\mathrm{z}} Y\sin\theta_{\mathrm{z2}}}{|\boldsymbol{v}_{\mathrm{z2p}}|^3} d\theta_{\mathrm{z2}} \right) \end{aligned} \tag{2}$$

where $\mu_0 = 4\pi \times 10^{-7}$; the number of turns $N_{\mathrm{x}} = 28$, $N_{\mathrm{y}} = 28$, $N_{\mathrm{z}} = 25$; $\boldsymbol{v}_{\mathrm{x1p}}$, $\boldsymbol{v}_{\mathrm{x2p}}$, $\boldsymbol{v}_{\mathrm{y1p}}$, $\boldsymbol{v}_{\mathrm{y2p}}$, $\boldsymbol{v}_{\mathrm{z1p}}$, and $\boldsymbol{v}_{\mathrm{z2p}}$ are the vectors from a point at $\mathrm{C_{X1}}$, $\mathrm{C_{X2}}$, $\mathrm{C_{Y1}}$, $\mathrm{C_{Y2}}$, $\mathrm{C_{Z1}}$, and $\mathrm{C_{Z2}}$ to $P(X,Y,Z)$, respectively; R_{x}, R_{y}, and R_{z} are the radii of $\mathrm{C_{XX}}$, $\mathrm{C_{YY}}$, and $\mathrm{C_{ZZ}}$, respectively; θ_{x1}, θ_{x2}, θ_{y1}, θ_{y2}, θ_{z1}, and θ_{z2} are the integral angles of the loops at the coils $\mathrm{C_{X1}}$, $\mathrm{C_{X2}}$, $\mathrm{C_{Y1}}$, $\mathrm{C_{Y2}}$, $\mathrm{C_{Z1}}$, and $\mathrm{C_{Z2}}$ to $P(X,Y,Z)$, respectively.

Based on (2), I_{x}, I_{y}, and I_{z} are all set to a current of 1 A, and the magnitude of the magnetic field in space is calculated to be (0.448, 0.448, 0.471) Gs at the origin O, i.e., $(B_{\mathrm{x}}, B_{\mathrm{y}}, B_{\mathrm{z}}) = 0.448(I_{\mathrm{x}}, I_{\mathrm{y}}, 1.051I_{\mathrm{z}})$. That is, the adjustment of the magnetic field in any direction is achieved by adjusting the magnitude and direction of I_{x}, I_{y}, and I_{z}. The direction is achieved by changing the phase angle to 0° or 180°. Since our transmitting coils are like Helmholtz coils, the difference in the magnetic field distribution in the central region is not very large. The difference in the magnetic field in the x-axis (or y-axis) is less than 7.6% in the distance from -50 mm to +50 mm from the origin O, and the difference in the magnetic field in the z-axis is less than 4.5% in the distance from -50 to +50 mm from the origin O. So, the like Helmholtz coils can generate a central region of nearly uniform magnetic field, and the difference in magnetic flux density in the central region is not significant (less than 7.6%).

B. Simulation of the Magnetic Field Distribution

In order to visualize the magnitude and direction of the magnetic field in relation to the drive currents in the transmitting coils, the software COMSOL is used for the simulation. The number of turns and the position of the transmitting coils in the simulation are set according to Section II-A. The magnetic field distribution is simulated for different drive currents, as shown in Fig. 5. It can be observed that the direction of the magnetic field distribution in the central area can be controlled using the current of each coil and that stronger the magnetic flux density is, the closer the coil wire is to the coil.

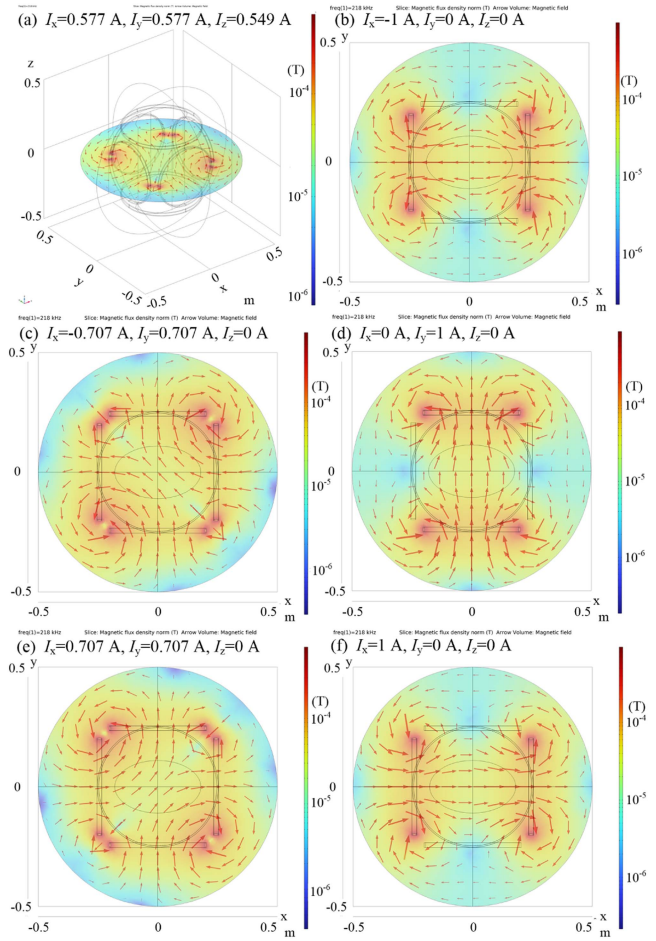

Fig. 5. Magnetic field distribution at different drive currents. (a) 3-D view when $I_x = 0.577$ A, $I_y = 0.577$ A, and $I_z = 0.549$ A. (b)–(f) $x - y$ plane views. (b) I_x = -1 A, $I_y = 0$ A, and $I_z = 0$ A. (c) I_x = -0.707 A, $I_y = 0.707$ A, and $I_z = 0$ A. (d) $I_x = 0$ A, $I_y = 1$ A, and $I_z = 0$ A. (e) $I_x = 0.707$ A, $I_y = 0.707$ A, and $I_z = 0$ A. (f) $I_x = 1$ A, $I_y = 0$ A, and $I_z = 0$ A.

From Fig. 5(a) to (f), all the arrows at the origin O are approximately the same length, meaning that the magnitude of the magnetic induction is nearly the same, which is consistent with the theoretical calculation at the origin O. The direction of magnetic induction at the origin O is the same as the vector $(I_x, I_y, 1.051I_z)$. This indicates that the magnetic field can be controlled in any direction in space by controlling the currents I_x, I_y, and I_z.

C. Measurement of the Magnetic Flux Density

To verify the validity of the principle and the simulation, a test of the magnetic field is carried out on the WPT system. An MC165 sensor (Magnetic Sciences) is placed at the origin O in the direction of the magnetic field to measure the magnetic flux density at each set of drive currents. Three current probes N2783B (Keysight) are used to measure the waveforms of I_x, I_y, and I_z. As shown in Fig. 6, the result shows that the magnitude of the magnetic flux density can be kept approximately constant and adjusted at any orientation by the adjustment of the current. The phase of the magnetic field lags behind the current probably due

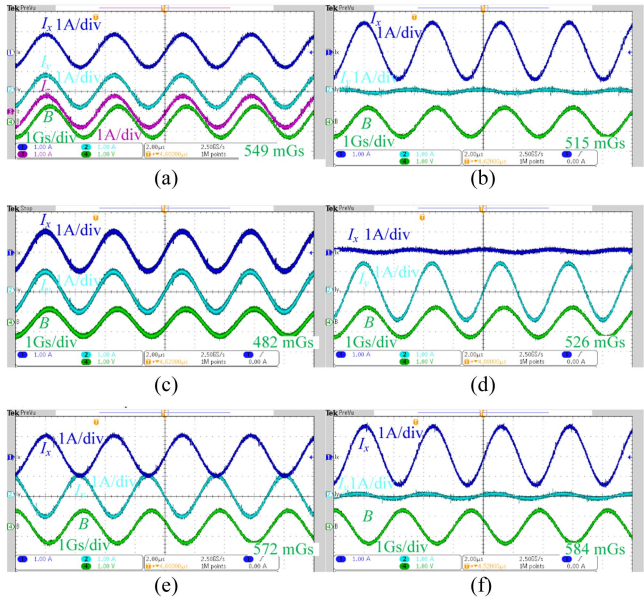

Fig. 6. Measurement of the magnetic flux density at different drive currents. (a) $I_x = 0.577$ A, $I_y = 0.577$ A, and $I_z = 0.549$ A. (b) $I_x = -1$ A, $I_y = 0$ A, and $I_z = 0$ A. (c) $I_x = -0.707$ A, $I_y = 0.707$ A, and $I_z = 0$ A. (d) $I_x = 0$ A, $I_y = 1$ A, and $I_z = 0$ A. (e) $I_x = 0.707$ A, $I_y = 0.707$ A, and $I_z = 0$ A. (f) $I_x = 1$ A, $I_y = 0$ A, and $I_z = 0$ A.

to the MC165 magnetic field sensor's characteristics. The output of the MC165 (B) is 1 Gs/div and its RMS value is approximately equal to the calculated and simulated results. For example, when $I_x = -1$ A, $I_y = 0$ A, and $I_z = 0$ A [see Fig. 6(b)], the desired $|B| = 0.448$ Gs and the measured $|B| = 0.515$ Gs. The source of the error could be the MC165's self-error or the manufacturing error in the 3DTC building process.

Through this part of the experiment, the characteristics of the 3DTC designed in this article are verified to be feasible for generating a magnetic field in any orientation to complete the WPT of a single receiving coil.

IV. Control of the WPT System

A. WPT Circuit Design

The WPT circuit is designed to control the current of each transmitting coil set. The inductance of C_{X1} and C_{X2} in series is L_{xx}, the inductance of C_{Y1} and C_{Y2} in series is L_{yy}, and the inductance of C_{Z1} and C_{Z2} in series is L_{zz}. R_{xx} is the resistance of L_{xx} at 218 kHz. It is significant to note that L_{xx}, L_{yy}, and L_{zz} are orthogonal at their sides. Therefore, there is a small mutual inductance between them. To reduce the effect of this small mutual inductance, the LCCL circuit is used because of its high-impedance characteristics [21]. The circuit diagram designed for the system is shown in Fig. 7. The 218-kHz voltage excited by L_{xx} from L_{yy} or L_{zz} will constitute a circuit with L_1 and C_1, which resonates at 218 kHz when the impedance is theoretically infinite. Therefore, in this case, the current of L_{xx} is not affected by the induced voltage and is only related to the drive circuit.

In addition, the current sensor for each axis consists of ACS70331 and LTC1968. The ACS70331 is a current sampling

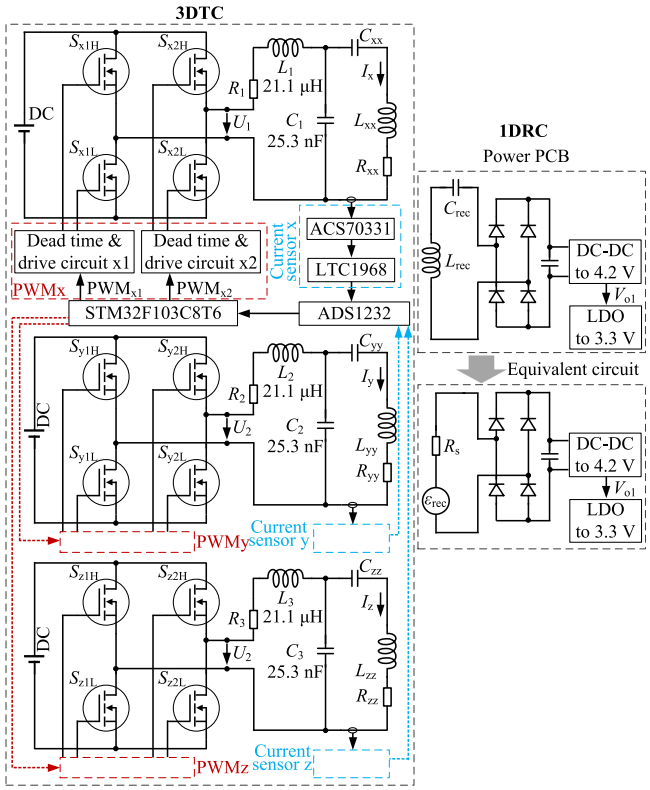

Fig. 7. Circuit diagram of the WPT system for the capsule.

chip, the LTC1968 converts the sampled current into a voltage signal, and the ADS1232 is a 24-high-precision ADC chip. S_{x1H}, S_{x1L}, S_{x2H}, and S_{x2L} are N-channel gallium nitride (GaN) transistors with a model of GS66508T. The dead time of the PWM driving the GaN transistors set by the dead circuit is 100 ns. The receiving coil on the capsule has an inductance of L_{rec}, which resonates with C_{rec} at 218 kHz, and the generated ac voltage is converted to dc by a full-bridge rectifier circuit and then to a battery charging voltage of 4.2 V by a dc–dc circuit.

According to Faraday's law, a controlled voltage source is induced in the receiving loop by the transmitting coil current. The voltage source is applied directly to the input port of the rectifier through the resonance of L_{rec} and C_{rec}. The voltage source ε_{x-rec} excited by the x-axial coil at the resonant frequency can be derived from the following equation:

$$\varepsilon_{x-rec} = j\omega M_{x-rec} I_x \tag{3}$$

where M_{x-rec} is the mutual inductance between L_{rec} and L_{xx}. The received voltage of the capsule ε_{rec} excited by all transmitting coils is the vector sum of the voltages excited by the x, y, and z axial coils. According to Faraday's law of electromagnetic induction and [13], the RMS of the total electromotive force excited by 3DTC can be described as

$$\varepsilon_{rec} = \frac{nS\omega\cos(\theta)\,|\boldsymbol{B}_p|\,k_c}{\sqrt{2}} \tag{4}$$

where n signifies the number of turns of the receiving coil, S represents the single-turn enclosed area, θ denotes the angle

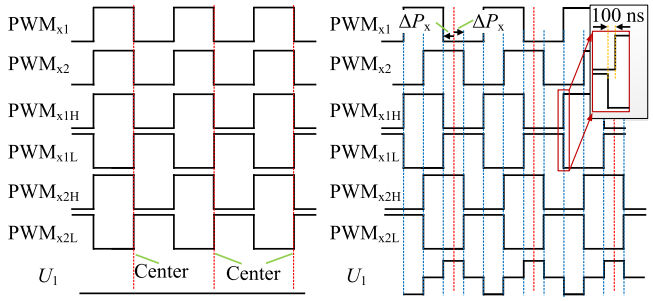

Fig. 8. Phase-shift control.

between the direction of the magnetic field and the central axis of the receiving coil, and k_c corresponds to the mutual inductance enhancement factor due to the presence of the ferrite ring. θ can be controlled to 0° or near 0° by controlling the currents of the 3DTC, benefiting from the fact that the attitude of the capsule endoscope can be obtained by the integrated IMU.

L_{rec} and C_{rec} can be equivalently described as a voltage source ε_{rms} in series with a resistor R_s. The relationship between the voltage source ε_{rms} and the output voltage V_{o1}, which is 4.2 V for recharging the battery and powering the 6 PCBs through the LDO can be expressed as [22], [23], [24]

$$\varepsilon_{rms} \approx \frac{2\sqrt{2}V_{o1}n_{dc}}{\pi\eta_{dc}} + \frac{4\sqrt{2}V_{FD}}{\pi} + \frac{\pi R_s V_{o1}}{2\sqrt{2}R_L n_{dc}} \tag{5}$$

where n_{dc} is the ratio of the input voltage to the output voltage of the dc–dc circuit, η_{dc} represents the efficiency of the dc–dc circuit, V_{FD} is the forward voltage drop of the rectifier diode, and R_L is the equivalent load of the WCE, specifically the equivalent of all the loads containing a battery and six PCBs.

B. Current Control

The equation for the transmitting coil current I_x at the resonant frequency of L_1 and C_1 is shown in (6), which is independent of the coupling and loading conditions [25]

$$I_x = \frac{U_1}{j\omega L_1}. \tag{6}$$

The angular frequency ω and the inductance L_1 are constant values, so we can control the current I_x by controlling the voltage U_1. As shown in Fig. 8, the control of the voltage U_1 can be achieved by phase-shifting control of the transistors. For the dead time and drive circuit x1, it inputs $\mathrm{PWM_{x1}}$ to output two signals $\mathrm{PWM_{x1H}}$ and $\mathrm{PWM_{x1L}}$ to drive transistors $\mathrm{S_{x1H}}$ and $\mathrm{S_{x1L}}$, which are inverted and have a 100-ns dead time to prevent short-circuiting of the dc supply due to simultaneous conduction of the two transistors. The phase and magnitude of the voltage U_1 can be controlled by controlling the phase of $\mathrm{PWM_{x1}}$ and $\mathrm{PWM_{x2}}$. The phase of $\mathrm{PWM_{x1}}$ moving left along the center line is ΔP_x, and the phase of $\mathrm{PWM_{x1}}$ moving right along the center line is also ΔP_x. Therefore, the voltage U_1 can be controlled by ΔP_x.

The difference between the set current I_{xset} and the measured current I_x is $e_x(t)$, that is, $e_x(t) = I_{xset} - I_x$. The control phase

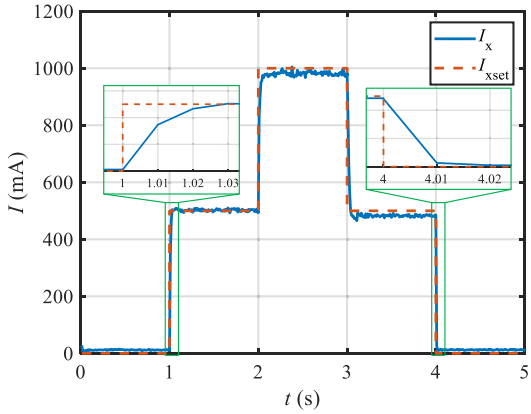

Fig. 9. Current control test where I_{xset} is the set current and I_x is the measured current controlled by the PID controller on the WPT system.

equation for the current closed loop is

$$\Delta P_x = K_{xp} e_x(t) + K_{xi} \int_0^t e_x(t)dt + K_{xd} \frac{de_x(t)}{dt} \quad (7)$$

where K_{xp}, K_{xi}, and K_{xd} are the proportional, integral, and differential coefficients, respectively.

C. Current Control Test of Transmitting Coil

For testing the effect of PID control on the current, the STM32 MCU used in this article controls the current at a control frequency of 100 Hz. The I_x current is set to 500 mA at 1 s, 1000 mA at 2 s, 500 mA at 3 s, and 0 mA at 4 s. As shown in Fig. 9, it can be seen that the rise time for 500 mA at 1 s is approximately 30 ms, and the fall time for 500 mA at 4 s is around 20 ms. So when there is a large rotation of the capsule attitude, the WPT system can track it quickly.

The accuracy of the independent control of the individual coil current is within 30 mA. This current control accuracy can meet the requirements of capsule WPT systems.

V. Experimental Verification

A. Capsule Endoscope WPT System

After the theoretical analysis and preliminary tests are completed, the prototype is built to carry out WPT experiments. As shown in Fig. 10, the current probes (Keysight N2783B) of the oscilloscope (DPO3034) are used to calibrate the current sensors (ACS70331 and LTC1968), and they are no longer required after the calibration has been completed. The capsule is fixed in a 3-D printed cuboid resin shell and then adjusted to a certain angle by the rotation of the servo motor for static WPT testing. The WCE self-adaptive tracking WPT is performed by adjusting the angular velocity of the servo motor at an angle interval. The measurement of the received power is to replace the full-bridge output of the WCE with a 100 Ω resistor, and directly measure the power on the 100 Ω resistor, which is the received power P_{rec} mentioned in this experiment.

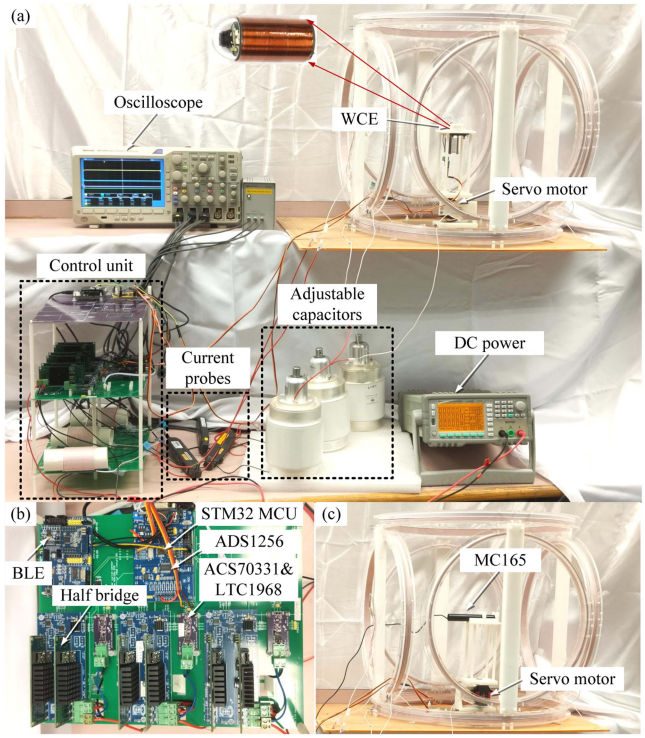

Fig. 10. System setup. (a) Whole system. (b) Control circuit PCB. (c) Setup of the magnetic field measurement.

TABLE IV
$x-y$ Plane Received Power Test

Degree (°)	I_x (mA)	I_y (mA)	I_{rec} (mA)	P_{rec} (mW)	P_{DC} (W)	η (%)
0	1000	0	124	1537.6	38	4.05
30	866	500	135	1822.5	40	4.56
60	500	866	133	1768.9	40	4.42
90	0	1000	130	1690.0	36	4.69
120	-500	866	135	1822.5	46	3.96
150	-866	500	130	1690.0	49	3.45
180	-1000	0	120	1440.0	50	2.88

B. Static WPT Experiment of Capsule Endoscope

In the static WPT experiment, the wireless charging power is tested by adjusting the angle of the servo in the $x-y$ or $x-z$ plane. The test data of the $x-y$ plane is shown in Table IV. When the $x-y$ transmitting coil is driven by a vector sum of RMS 1 A currents generating a magnetic flux density of 0.448 Gs at the origin O, the average received power of the capsule in the $x-y$ plane is 1681.6 mW and the average received current is 129.6 mA, ranging from 120 to 135 mA. The reason for the fluctuations in received current may be that the winding of the coil as a nonideal coil causes small differences in coupling in each direction. The maximum efficiency measured from the dc supply to the 100 Ω resistor is 4.69%. The low PTE is due to the fact that the transmitting coil is much larger in diameter than the receiving coil and is far away. In addition, some of the energy is absorbed by the transmitting coils in the other axes.

TABLE V
$x-z$ PLANE RECEIVED POWER TEST

Degree (°)	0	30	60	90	120	150	180
I_{rec}(mA)	125	120	115	116	110	114	120
P_{rec}(mW)	1562.5	1440.0	1322.5	1345.6	1210.0	1299.6	1440.0

The received power test data for the $x-z$ plane is shown in Table V. $x-z$ plane has an average received power of 1374.3 mW and an average received current of 117.1 mA, ranging from 110 to 125 mA. Its characteristics are similar to those of the $x-y$ plane. The difference in average received current between the $x-y$ and $x-z$ planes is 12.5 mA, perhaps because the positions are not perfectly aligned, or because of the nonideal winding of the coils.

This part of the experimental test demonstrates that the charging current of the capsule can be kept approximately constant in space. The average received current of $x-y$ and $x-z$ planes is 123 mA, and the corresponding power is 1512.9 mW, which is much larger than the 420 mW power required by the multitasking capsule.

C. Self-Adaptive WPT Experiment of Capsule Endoscope

The purpose of self-adaptive WPT is to achieve constant power tracking. When the capsule is inside the human body, it will be affected by the stomach peristalsis and its attitude will change. If the transmitting currents are kept constant, the charging power and efficiency will drop due to the effect of the peristalsis. In order to prevent this situation, the attitude of the capsule is measured in real time by the IMU, and self-adaptive WPT is achieved by adjusting the magnitude and the positive and negative of the transmitting currents so that the direction of the magnetic field is aligned with the axial direction of the 1DRC. In addition, the value of the constant power is adjustable according to the power consumption of the capsule endoscope.

In the self-adaptive WPT experiment, the angle and velocity of the capsule endoscope are adjusted by the servo motor, and the dynamic attitude information measured by the capsule's IMU is transmitted in real-time via Bluetooth to the STM32 MCU, which calculates the current decomposed to each axis and controls the current of each axis to complete the self-adaptive charging of the capsule endoscope. The self-adaptive WPT test of the $x-y$ plane is shown in Fig. 11. The angular velocity of the servo motor is -180 °/s, 180 °/s, -45 °/s, or 45 °/s. It can be seen from Fig. 11 that the received current may drop more instantaneously at ± 180 °/s, which may be caused by the delay of Bluetooth transmission. In Fig. 11(a), the desired received current is 123 mA, and the measured received current fluctuates around 125 mA. The desired received current of Fig. 11(c) is 98 mA, and the actual measured received current fluctuates around 100 mA. The YAW angle obtained from the IMU can only be from integrated angular velocity data, so the cumulative error will become larger and larger over time.

The self-adaptive WPT test in the $x-z$ plane is shown in Fig. 12. In Fig. 12(a), the desired received current is 123 mA,

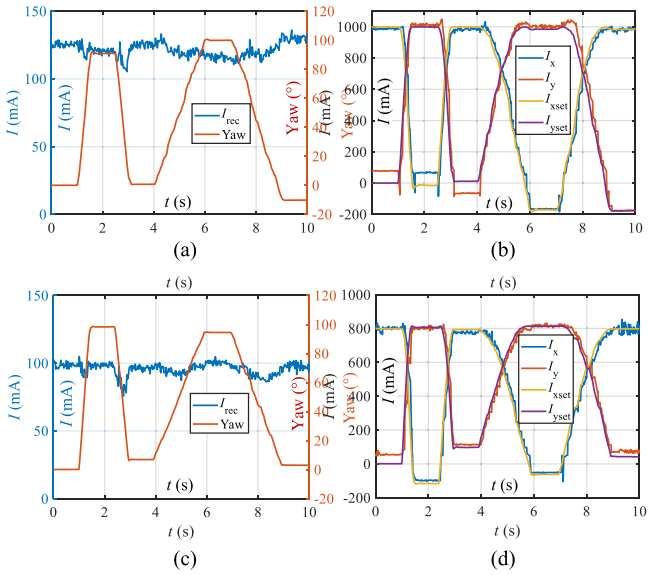

Fig. 11. $x-y$ plane self-adaptive WPT experiment. (a) Desired received current 123 mA ($P_{\mathrm{rec}} = 1512.9$ mW). (b) Currents of the corresponding transmitting coils for (a). (c) Desired received current 98 mA ($P_{\mathrm{rec}} = 960.4$ mW). (d) Currents of the corresponding transmitting coils for (c).

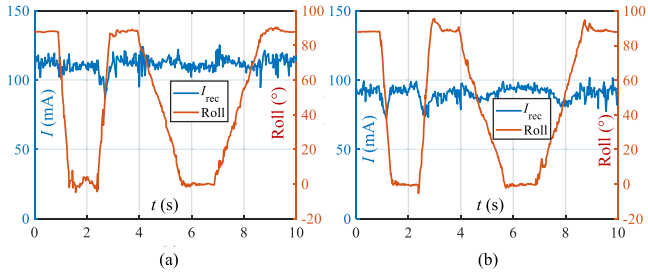

Fig. 12. $x-z$ plane self-adaptive WPT experiment. (a) Desired received current 123 mA. (b) Desired received current 98 mA.

and the measured received current fluctuates around 117 mA. The desired received current of Fig. 12(b) is 98 mA, and the actual measured received current fluctuates around 95 mA. The roll angle from the IMU is obtained by integrating the angular velocity and fused with the measured processing of the acceleration of gravity, so its error is almost independent of time [27]. However, when the angular velocity changes quickly, the measurement error of the acceleration of gravity will be caused by vibration, so the ROLL angle has a large error at the angular velocity inflection point.

VI. DISCUSSION

The comparison with the existing WPT system for capsules is shown in Table VI. It can be seen that the received power of our WCE is much larger than the received power of the previous studies, and it can be adjusted to a specified value of received power. In previous studies, many researchers used a 3DRC and a 1DTC [11], [16], [26], [28], which take up most of the volume of the capsule, so it is essential to investigate a 1-D receive coil.

TABLE VI
COMPARISON WITH EXISTING WPT SYSTEM FOR CAPSULES

Study	Transmitting coil		Receiving coil		Frequency	P_L (mW)	Efficiency η
	Type	Size (cm)	Type	Size (mm)			
[26]	1DTC	ϕ40	3DRC	ϕ10×12	400 kHz	750	≥1.24%
[11]	1DTC	Square: 40×40	3DRC	ϕ12.8×14	218 kHz	651	≤8.68%
[16]	1DTC	ϕ35	3DRC	ϕ12×12	250 kHz	758 −920	≥8.21%
[13]	Rotatable 2DTC	ϕ40×20, ϕ49×24.5	1DRC	ϕ(10−13) ×15	218 kHz	500	8.15%–13.53%
This article	3DTC	ϕ40×48.8, ϕ40×48.8, ϕ50×48	1DRC	ϕ13×20	218 kHz	1210 −1822.5	4.69%

Compared with the work in [13], our 3DTC has the space to accommodate a human body with higher transmission power and has no mechanical motion mechanism allowing control of the magnetic field to a specified magnitude and direction within 30 ms. Since our coil is not a Helmholtz coil whose distance from the coil on the same axis (x-, y-, or z-axis) is much greater than the coil radius, the efficiency is lower than in [13]. In recent research, pulse frequency modulated (PFM) can be used to improve the efficiency of WPT [29]. The PFM is achieved by selecting two optimal fundamental or subharmonic frequencies $f_{2n\pm1} = f_{\text{key}}/(2n \pm 1)$ and then performing regular modulation between them. For the WPT of WCEs, we are more concerned with the receiving power P_L on the load, as the receiving efficiency of a capsule is difficult to achieve high due to the huge size difference between the receiving and transmitting coils and the long transmission distances while the receiving power is extremely important for the operation of the WCE. When it comes to the cumulative errors of the Yaw angle, which can be eliminated by the 6-D localization method [27]. Regarding the frequency, Khan et al. [30] mentioned that higher frequencies increase the absorption of human tissues, which may cause damage to the human body. In the literature review [31], 218 kHz or around is one of the popular frequencies for WPT using the Helmholtz coil. Therefore, the 218 kHz frequency is chosen in this work.

Experiments in the air have been completed with promising results, but the application in the human body still needs to be studied, and the experiment in the animal body needs to be completed first. Based on the ICNIRP guidelines [32], [33], electric field E and SAR must be taken as the 99th percentile or averaged in 10 g of continuous tissue, respectively [34]. The calculated restrictions are $E = 20.81$ V/m and SAR $= 2$ W/kg at the resonant frequency of 218 kHz. According to the work in [34], [35], and [36], a COMSOL simulation model is established for the safety of electric field E and SAR, and an elliptical column is used to mimic the human body. As shown in Fig. 13, the maximum SAR is 6.5 mW/kg, which is less than 2 W/kg and the maximum electric field E is around 6 V/m, which is also less than the restricted electric field E of 20.81 V/m. Therefore, the preliminary study of the system using COMSOL is safe to use in terms of SAR and electric field limits. However, more investigation and clinical measurement are needed in the future. In addition, to ensure a safe temperature rise, the temperature of the receiving coil is required to be below 42.5 °C [37], which can be achieved by increasing the heat dissipation capacity of the 1DRC and regulating the induction power.

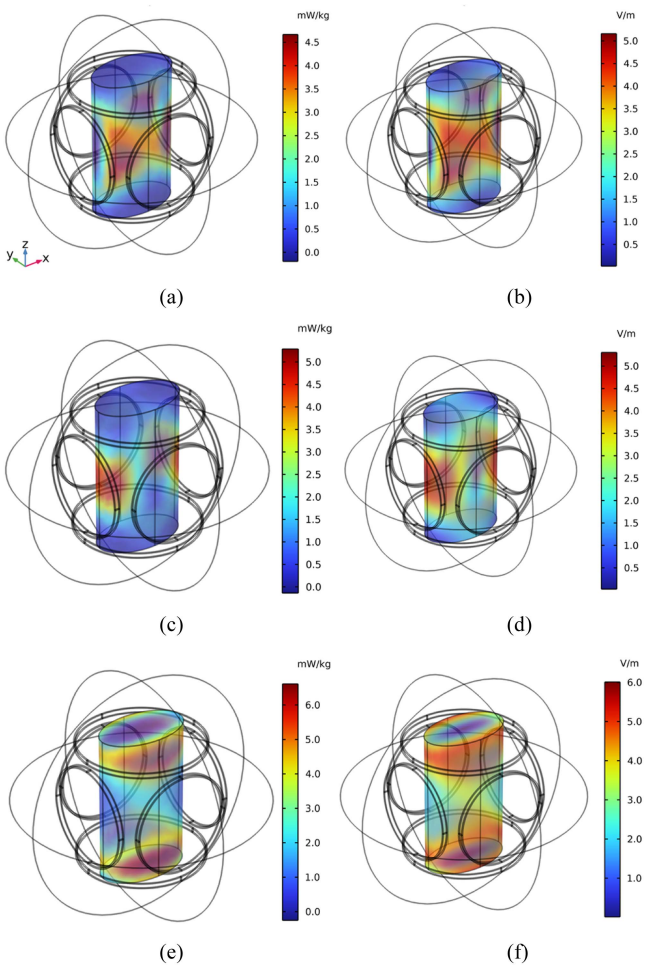

Fig. 13. Simulation SAR and electric field E in the human body model.

VII. CONCLUSION

This article describes the design, implementation, and tests of a WCE system with self-adaptive wireless power control. The model analysis and magnetic field simulation of the system are presented, followed by the discussion of the circuit design, control implementation, and structure fabrication. It is important to note that the system is a full-size structure and tests are carried out to emulate the movement of peristalsis. Experimental results confirmed that the proposed adaptive control method is able to respond to the WCE rotation and regulate the received power by controlling the transmitters' excitation. When the WCE is

located at the center of the structure, which is the lowest level of the magnetic flux density along the axial direction, the system efficiency is approximately 4.69%.

APPENDIX
TURNS DESIGN OF WPT

In order to find the optimal number of coils C_{X1} and C_{X2} turns to achieve the highest or near highest transmission efficiency, the transmitting coil C_{XX} with different numbers of turns is tested as given in Table VII, where R_{eq} is the equivalent load resistance at

TABLE VII
RELATIONSHIP BETWEEN THE NUMBER OF TURNS OF COILS C_{X1} AND C_{X2} AND TRANSMISSION EFFICIENCY

$N_{C_{X1}} = N_{C_{X2}}$	I_x (A)	U_x (V)	I_{rec} (mA)	R_{eq} (Ω)	η (%)
27	0.5	11.35	61.47	100	6.77
28	0.5	13.13	73.31	100	8.38
29	0.5	15.28	79.08	100	8.33

the 1DRC output. The efficiency η does not increase significantly after 28 turns, so we selected a coil turn number of 28 turns in the x-axis. The efficiency here is much higher than that in Table IV because the y and z axes coils are in an open circuit and there is no energy loss in the y and z axes coils. Although the x, y, and z axes coils of the transmitting coils are orthogonal, there is still a small mutual inductance and the *LCCL* circuit is not ideal not completely open for the transmitting coils, so there is a certain amount of energy loss in the y and z axes coils when the transmitting coil in the x-axis is driven with current. The parameters design in the y-axis direction is exactly the same as that in the x-axis direction and the parameters design in the z-axis direction is similar to the design method in the x-axis direction.

ACKNOWLEDGMENT

The authors would like to thank Dr. Wei Liu, Dr. Jiali Zhou, and Dr. Liangxi He for their assistance in the experiments.

REFERENCES

[1] H. Sung et al., "Global cancer statistics 2020: GLOBOCAN estimates of incidence and mortality worldwide for 36 cancers in 185 countries," *CA: Cancer J. Clinicians*, vol. 71, no. 3, pp. 209–249, 2021.
[2] T. Gan, S. Liu, J. Yang, B. Zeng, and L. Yang, "A pilot trial of convolution neural network for automatic retention-monitoring of capsule endoscopes in the stomach and duodenal bulb," *Sci. Rep.*, vol. 10, no. 1, pp. 1–10, 2020.
[3] R. A. Enns et al., "Clinical practice guidelines for the use of video capsule endoscopy," *Gastroenterology*, vol. 152, no. 3, pp. 497–514, 2017.
[4] P. Magalhães-Costa, M. Bispo, S. Santos, G. Couto, L. Matos, and C. Chagas, "Re-bleeding events in patients with obscure gastrointestinal bleeding after negative capsule endoscopy," *World J. Gastrointestinal Endoscopy*, vol. 7, no. 4, 2015, Art. no. 403.
[5] K. Mergener, "Update on the use of capsule endoscopy," *Gastroenterol. Hepatol.*, vol. 4, no. 2, 2008, Art. no. 107.
[6] A. Liaqat, M. A. Khan, J. H. Shah, M. Sharif, M. Yasmin, and S. L. Fernandes, "Automated ulcer and bleeding classification from WCE images using multiple features fusion and selection," *J. Mechanics Med. Biol.*, vol. 18, no. 4, 2018, Art. no. 1850038.
[7] M. A. Khan et al., "Computer-aided gastrointestinal diseases analysis from wireless capsule endoscopy: A framework of best features selection," *IEEE Access*, vol. 8, pp. 132850–132859, 2020.
[8] A. Moglia, A. Menciassi, P. Dario, and A. Cuschieri, "Capsule endoscopy: Progress update and challenges ahead," *Nature Rev. Gastroenterol. Hepatol.*, vol. 6, no. 6, pp. 353–361, 2009.
[9] M. F. Hale, R. Sidhu, and M. E. McAlindon, "Capsule endoscopy: Current practice and future directions," *World J. Gastroenterol.: WJG*, vol. 20, no. 24, 2014, Art. no. 7752.
[10] M. R. Basar, M. Y. Ahmad, J. Cho, and F. Ibrahim, "Application of wireless power transmission systems in wireless capsule endoscopy: An overview," *Sensors*, vol. 14, no. 6, pp. 10929–10951, 2014.
[11] Y. Meng et al., "A novel wireless power transfer system with two parallel opposed coils for gastrointestinal capsule robot," *Sensors Actuators A: Phys.*, vol. 321, 2021, Art. no. 112413.
[12] Z. Jia, G. Yan, H. Liu, Z. Wang, P. Jiang, and Y. Shi, "The optimization of wireless power transmission: Design and realization," *Int. J. Med. Robot. Comput. Assist. Surg.*, vol. 8, no. 3, pp. 337–347, 2012.
[13] J. Gao et al., "Stable wireless power transmission for a capsule robot with randomly changing attitude," *IEEE Trans. Power Electron.*, vol. 38, no. 2, pp. 2782–2796, Feb. 2023.
[14] T. Sun, X. Xie, G. Li, Y. Gu, Y. Deng, and Z. Wang, "A two-hop wireless power transfer system with an efficiency-enhanced power receiver for motion-free capsule endoscopy inspection," *IEEE Trans. Biomed. Eng.*, vol. 59, no. 11, pp. 3247–3254, Nov. 2012.
[15] M. R. Basar, M. Y. Ahmad, J. Cho, and F. Ibrahim, "Stable and high-efficiency wireless power transfer system for robotic capsule using a modified Helmholtz coil," *IEEE Trans. Ind. Electron.*, vol. 64, no. 2, pp. 1113–1122, Feb. 2017.
[16] M. R. Basar, M. Y. Ahmad, J. Cho, and F. Ibrahim, "An improved wearable resonant wireless power transfer system for biomedical capsule endoscope," *IEEE Trans. Ind. Electron.*, vol. 65, no. 10, pp. 7772–7781, Oct. 2018.
[17] W. M. Ng, C. Zhang, D. Lin, and S. R. Hui, "Two-and three-dimensional omnidirectional wireless power transfer," *IEEE Trans. Power Electron.*, vol. 29, no. 9, pp. 4470–4474, Sep. 2014.
[18] S. Anjani, Y. Song, T. Hou, I. A. Ruiter, and P. Vink, "The effect of 17-inch-wide and 18-inch-wide airplane passenger seats on comfort," *Int. J. Ind. Ergonom.*, vol. 82, 2021, Art. no. 103097.
[19] C.-Y. Li, B.-L. Zhang, C.-X. Chen, and Y.-M. Li, "OMOM capsule endoscopy in diagnosis of small bowel disease," *J. Zhejiang Univ. Sci. B*, vol. 9, pp. 857–862, 2008.
[20] H. Zhuang, W. Wang, K. Zhao, S. Kuang, Z. Wang, and G. Yan, "Efficient power receiving coil with novel ferrite core structure for capsule robot," *IEEE Trans. Biomed. Circuits Syst.*, vol. 16, no. 5, pp. 939–946, Oct. 2022.
[21] J. Feng, Q. Li, F. C. Lee, and M. Fu, "LCCL-LC resonant converter and its soft switching realization for omnidirectional wireless power transfer systems," *IEEE Trans. Power Electron.*, vol. 36, no. 4, pp. 3828–3839, Apr. 2021.
[22] A. P. Hu, "Selected resonant converters for IPT power supplies," Ph.D. dissertation, Dept. Elect. Electron. Eng., Univ. Auckland, Auckland, New Zealand, 2001.
[23] J. Gao, G. Yan, Z. Wang, P. Jiang, and D. Liu, "A capsule robot powered by wireless power transmission: Design of its receiving coil," *Sensors Actuators A: Phys.*, vol. 234, pp. 133–142, 2015.
[24] Y. Li et al., "Analysis, design, and experimental verification of a mixed high-order compensations-based WPT system with constant current outputs for driving multistring LEDs," *IEEE Trans. Ind. Electron.*, vol. 67, no. 1, pp. 203–213, Jan. 2020.
[25] J. Feng, Q. Li, and F. C. Lee, "Coil and circuit design of omnidirectional wireless power transfer system for portable device application," in *Proc. IEEE Energy Convers. Congr. Expo.*, 2018, pp. 914–920.
[26] W. Xin, G. Yan, and W. Wang, "Study of a wireless power transmission system for an active capsule endoscope," *Int. J. Med. Robot. Comput. Assist. Surg.*, vol. 6, no. 1, pp. 113–122, 2010.
[27] H. Zhang, Y. Li, and Z. Li, "6-D spatial localization of wireless magnetically actuated capsule endoscopes based on the fusion of hall sensor array and IMU," *IEEE Sensors J.*, vol. 22, no. 13, pp. 13424–13433, Jul. 2022.
[28] J. Gao et al., "Design and optimization of a novel double-layer Helmholtz coil for wirelessly powering a capsule robot," *IEEE Trans. Power Electron.*, vol. 39, no. 1, pp. 1826–1839, Jan. 2024.
[29] W. Liu, K. Chau, C. H. Lee, W. Han, X. Tian, and W. Lam, "Full-range soft-switching pulse frequency modulated wireless power transfer," *IEEE Trans. Power Electron.*, vol. 35, no. 6, pp. 6533–6547, Jun. 2020.
[30] S. R. Khan, S. K. Pavuluri, G. Cummins, and M. P. Desmulliez, "Miniaturized 3-D cross-type receiver for wirelessly powered capsule endoscopy," *IEEE Trans. Microw. Theory Techn.*, vol. 67, no. 5, pp. 1985–1993, May 2019.

[31] Y. Zhou, C. Liu, and Y. Huang, "Wireless power transfer for implanted medical application: A review," *Energies*, vol. 13, no. 11, 2020, Art. no. 2837.
[32] International Commission on Non-Ionizing Radiation Protection et al., "Guidelines for limiting exposure to electromagnetic fields (100 kHz to 300 GHz)," *Health Phys.*, vol. 118, no. 5, pp. 483–524, 2020.
[33] International Commission on Non-Ionizing Radiation Protection et al., "Guidelines for limiting exposure to time-varying electric and magnetic fields (1 Hz to 100 kHz)," *Health Phys.*, vol. 99, no. 6, pp. 818–836, 2010.
[34] T. Campi, S. Cruciani, F. Maradei, and M. Feliziani, "A new transmitting coil for powering endoscopic capsules using wireless power transfer," *Electronics*, vol. 12, no. 8, 2023, Art. no. 1942.
[35] F. Chen, P. Jiang, G. Yan, W. Wang, and Y. Meng, "Design of multi-coil wireless power transfer system for gastrointestinal capsule robot," *J. Shanghai Jiaotong Univ. (Sci.)*, vol. 26, pp. 76–83, 2021.
[36] T. Campi, S. Cruciani, F. Maradei, and M. Feliziani, "Innovative wireless charging system for implantable capsule robots," *IEEE Trans. Electromagn. Compat.*, vol. 63, no. 5, pp. 1726–1734, Oct. 2021.
[37] K. Shiba, A. Morimasa, and H. Hirano, "Design and development of low-loss transformer for powering small implantable medical devices," *IEEE Trans. Biomed. Circuits Syst.*, vol. 4, no. 2, pp. 77–85, Apr. 2010.

Heng Zhang (Graduate Student Member, IEEE) received the B.Eng. and M.Eng. degrees in electrical engineering and automation from the Taiyuan University of Technology, Taiyuan, China, in 2017 and 2020, respectively. He is currently working toward the Ph.D. degree in electrical and electronic engineering from The University of Hong Kong, Hong Kong.

From 2021 to 2022, he was a Research Assistant with the Chinese University of Hong Kong, Hong Kong. His research interests include wireless power transfer, design, sensing, and control of medical robots.

Zheng Li (Senior Member, IEEE) received the B.Eng. and M.Eng. degrees in mechanical and automation engineering from Beihang University, Beijing, China, in 2007 and 2010, respectively, and the Ph.D. degree in robotics from The Chinese University of Hong Kong, Hong Kong, in 2013.

He is currently an Associate Professor with the Department of Surgery, Chow Yuk Ho Technology Centre for Innovative Medicine, Li Ka Shing Institute of Health Science, and Multi-scale Medical Robotics Centre, Ltd., The Chinese University of Hong Kong, Hong Kong. His research interests include design, kinematic modeling, sensing, and control of flexible and soft robots for medical applications.

Dr. Li is a member of ASME, RAS, and EMBS.

Chi-Kwan Lee (Senior Member, IEEE) received the B.Eng. and Ph.D. degrees in electronic engineering from the City University of Hong Kong, Kowloon, Hong Kong, in 1999 and 2004, respectively.

He is currently an Associate Professor with the Department of Electrical and Electronic Engineering, The University of Hong Kong, Hong Kong. He was a Lecturer in electrical engineering with Hong Kong Polytechnic University, Hung Hom, Hong Kong. From 2010 to 2020, he was a Visiting Researcher with Imperial College London, U.K. His current research interests include inductive power transfer, metamaterials for wireless power, and application of machine learning in the design of electromagnetic devices.

Dr. Lee was a recipient of the 2015 IEEE Power Electronics Society Transactions First Prize Paper Award for his publications on Wireless Power Transfer. He serves on the steering committee and was the General Chair of the 2018 IEEE PELS Workshop on Emerging Technologies: Wireless Power (WoW). He is an Associate Editor for IEEE TRANSACTIONS ON POWER ELECTRONICS and IEEE JOURNAL OF EMERGING AND SELECTED TOPICS IN POWER ELECTRONICS.